Acid washing of mnox-sba-15 composites as an efficient way to improve catalytic properties in hcho total oxidation

Guillaume Rochard, Sebastien Royer, Jean-Marc Giraudon, Jean-Francois Lamonier

Acid washing of MnOx - SBA-15 composites as an efficient way to improved catalytic properties in HCHO total oxidation

Guillaume Rochard, [a] Sébastien Royer, [a] Jean-Marc Giraudon, * [a] Jean-François Lamonier[a]

[a] Dr. G. Rochard, Dr. S. Royer, Dr. J.-M. Giraudon, Dr. J.-F. Lamonier
Univ. Lille, CNRS, Centrale Lille, ENSCL, Univ. Artois, UMR 8181
Unité de Catalyse et Chimie du Solide
F-59000 Lille, France
E-mail: jean-marc.giraudon@univ-lille.fr

Supporting information for this article is given via a link at the end of the document.

Abstract: The effect of HNO_3 10M treatment on MnOx nanoparticles mostly confined inside the porous channels of SBA-15 with low Mn average oxidation state (Mn AOS < 3) has been investigated on the physico-chemical properties of the catalysts as a function of Mn loading (10, 20, 30 wt%) to be tested in the total oxidation of formaldehyde. The acid-treated catalysts were extensively characterized (ICP, N_2-sorptions, H_2-TPR, TGA/DSC, HRTEM and XPS). It is found that the acid treatment promotes the redox and textural properties of the catalyts. Such property improvements allow to get more efficient catalysts in total oxidation of HCHO. Indeed, the standardized rate rs expressed as mmoles of formaldehyde converted into CO_2 per mole of Mn per hour at 130 °C increases by 5 and by 4 for the 20 wt% Mn and 30 wt% Mn based catalysts, respectively.

Introduction

Formaldehyde (HCHO) is considered as a dangerous volatile organic compound (VOC), mostly used in wood industry, as a glue component. As a consequence, HCHO is found in non-industrial indoor environment due to the degradation of this glue with time. Formaldehyde has been classified as a carcinogenic species and a prolonged exposure to HCHO contributes to important health issues (burning sensation, breath problem, cancers) [1]. As a consequence, removal of HCHO from indoor environment becomes a necessity. Among the different methods for HCHO removal, oxidation of HCHO into harmless species such as H_2O and CO_2 with low energy consumption through heterogeneous catalysis seems an effective and promising way for HCHO elimination [2]. Several studies have been carried out using efficient supported noble metal catalysts such as Pt/Ferrihydrite [3], Pd/TiO_2 [4] and Au/CeO_2 [5]. However, transition metal oxides (TMO) have attracted significant attention as potential substitutes of noble metal based catalysts which have the disadvantages to be expensive and of limited availability. Among the different TMO, MnO_2 which is inexpensive, readily available and environment friendly has exhibited promising performances in such reaction [6]. MnO_2 has been used as active support [7] [8] [9], bulk catalyst [10] [11] and most recently as an active supported phase [12] [13] for the catalytic formaldehyde oxidation.

As previously reported, the addition of manganese using $Mn(NO_3)_2.4H_2O$ as Mn(II) precursor, either by incipient wet impregnation (IWI) or melt infiltration (MI) [14] followed by a subsequent calcination step at 300°C induces differences in the location of the MnO_x particles. As the IWI route leads to the greater amount of MnO_x particles to be exposed on the outside of the carrier, on contrary, the MI route allows to get a significant amount of MnO_x particles located inside the mesoporous channels of the SBA-15 carrier.

In order to increase the amount of TMO particles (TM : Cu, Ni, Co) within the porosity of the mesoporous silica, a modified MI method has been recently performed taking full advantage of the confined space between the silica wall and the template aggregates in an as-prepared SBA-15 (SBAa) [15] [16] [17] [18] [19].

Taking these previous results into account, this modified MI has been recently validated in the case of manganese using $Mn(NO_3)_2.4H_2O$ as precursor [20]. However, the subsequent static calcination at 300 °C for 6 h gives rise to a Mn AOS of about 2.6 for sample with Mn loading of 20 wt.% in line with the detection of crystallized Mn_3O_4 as MnO_x species by XRD. This unexpected low Mn AOS, taking into account the low temperature of calcination [21], highlights the role of the template decomposition products which act as reductants toward MnO_x particles in the course of the calcination step [22] [23]. However, it has been previously found that the total oxidation of formaldehyde, without considering Mn dispersion, is enhanced over supported MnO_x with an average Mn valence close but less than 4 [24].

An easy way to raise the Mn AOS can be achieve through acid treatment on Mn^{3+} containing MnO_x (Mn_2O_3, Mn_3O_4 ($Mn^{3+}Mn_2^{2+}O_3$), γ-MnOOH) taking advantage of the disproportionation of Mn^{3+} to give soluble Mn^{2+} and MnO_2 as solid. Such strategy using wet method was carried out long time ago to get chemically activated manganese dioxide knowing that MnO_2 possesses numerous polymorphs. These types of transformations are very complex and the nature of the final MnO_2 polymorph is dependent among other things on various parameters such as the phase and O/Mn stoichiometry of the starting low valence Mn oxides, the type of acid, concentration, duration, temperature (ambient or T < 100°C) [25] [26] [27]. Acid treatment has been also reported to be a valuable treatment enabling an improvement of the textural properties of the metal oxide [28] [29].

Such a strategy was applied by our team to a mixture of Mn_3O_4 and Mn_2O_3 samples using H_2SO_4 (10 $mol.L^{-1}$) as acid reagent [30] to form after calcination at 300 °C the metastable layered structured Mn_5O_8 ($Mn_2^{2+}Mn_3^{4+}O_8$; Mn AOS : 3.2) with better textural properties. This resulting mixed oxide was shown to be more catalytically active in total oxidation of formaldehyde than the starting oxide mixture. Although enhancement of Mn AOS was achieved after acidic treatment, the transformation of Mn_3O_4/Mn_2O_3 into MnO_2 was not observed in that case taking into account of the Mn AOS of 3.4. In this regard, Mn_3O_4 dispersed in SBA-15 provides an interesting model system to study the effect of acid treatment on the location and nature of the new generated supported manganese oxide particles to optimize the physico-

chemical properties of the catalysts in the total oxidation of HCHO.

In this work the effect of an acid treatment using HNO_3 10M as reagent source has been investigated on MnOx/SBAa samples synthesized through the modified MI method. It should be noted that the effect of Mn loading (10, 20, 30 wt%) has been particularly investigated on the physico-chemical properties of the acid-treated materials to be discussed regarding the catalytic performances in the total oxidation of formaldehyde.

Results and Discussion

1. Acid Treatment

As reported previously [20] the modified MI method using a host support such as SBAa allows to get Mn_3O_4 particles predominantly located into the porous channels of the as made silica after static calcination at 300 °C for 6 h. Despite the low temperature of calcination, MnO_2 formation is precluded due to the presence of P123 degradation organic by-products acting as reductants towards manganese species. However, as previously reported, a Mn AOS close to 4 is beneficial for HCHO total oxidation [31]. In order to improve the Mn AOS an acid treatment was performed on the xMn-MIa catalysts. Such a treatment consists of an exposure of the fresh catalysts to a 10 M HNO_3 solution for 5 h at 25 °C. In those conditions, the enhancement of the Mn AOS is expected to occur taking advantage of the ease of Mn^{3+} (contained in Mn_3O_4) disproportionation to get Mn^{4+} (solid) and aqueous Mn^{2+} according to the formal equation:

$Mn_3O_4(s) + 4\ H^+(aq) \rightarrow MnO_2(s) + 2\ Mn^{2+}(aq) + 2\ H_2O\ (l)$ **Equation 1**

The effect of the acid treatment on the amount of manganese released into the solution was evaluated by elemental analysis (see **Table 1**). The release of manganese as $Mn^{2+}(aq)$, quantified in terms of Mn atomic percentage, amounts to 68 % for 20 wt% and 30 wt% Mn loading in perfect accordance with the expected value of 67 % considering the stoichiometry of the above equation. However, a higher value of 75 % is obtained for the less Mn loaded catalyst which will be discussed later. To conclude, based on relative Mn loss given by elemental analysis, it is found that the Mn solubilized amount is consistent with equation 1 for the xMn-MIa samples (x = 20; 30).

In **Table 1** are reported the structural and textural properties of the support and of the Mn based samples before and after acid treatment.

Table 1: Structural and textural properties of silica support, xMn-MIa and xMn-MIa-AT samples

Samples	Mn (wt%)	Mn phase	Dc [a] (nm)	S_{BET} (m^2/g)2	Vp [b] (cm^3/g)	Sμ [b] (m^2/g)	Vμ [b] (cm^3/g)	Dp [c] (nm)
SBAa	-	-	-	366 (627)	0.70 (1.20)	-	-	6.6
SBAc	-	-	-	827	1.20	233	0.03	7.3
10Mn-MIa	9.4	-		578 (672)	0.89 (1.03)	151 (176)	0.01 (0.01)	7.1
20Mn-MIa	19.2	Mn_3O_4	9	527 (737)	0.77 (1.08)	135 (189)	0.01 (0.01)	5.0 – 7.2
30Mn-MIa	26.6	Mn_3O_4	9	435 (720)	0.69 (1.14)	119 (197)	0.01 (0.01)	4.9 – 7.6
10Mn-MIa-AT	2.4	ε-MnO_2	-	828 (860)	1.31 (1.36)	247 (257)	0.04 (0.04)	7.1
20Mn-MIa-AT	6.1	ε-MnO_2	9	789 (874)	1.09 (1.21)	219 (243)	0.03 (0.03)	4.6 – 7.1
30Mn-MIa-AT	8.6	ε-MnO_2	9	610 (706)	0.84 (0.97)	189 (219)	0.03 (0.03)	4.6 – 7.2

[a] : crystallite size; [b] : in m^2 or cm^3 / $gSiO_2$; [c] : maximum pore diameter

2. Structural properties – X- ray diffraction

Figure 1 exhibits the XRD patterns of the acid-treated samples and those of the fresh catalysts for sake of comparison. The XRD patterns of the fresh samples are consistent with the presence of tetragonal hausmannite (Mn_3O_4, JCPDS 80-0382) phase except for the 10Mn-MIa for which the XRD pattern shows a large peak positioned between 15 to 30 ° in 2θ related to the amorphous silica and only weak fluctuation in the baseline at the awaited positions for the hausmannite phase. After acid treatment, whatever the XRD pattern under concern, all the diffraction peaks belonging to the parent hausmannite disappear totally while 4 new broad peaks located at 2θ = 37.1°, 42.4 °, 56.2 °, and 66.7 ° can be identified (20Mn-MIa-AT and 30Mn-MIa-AT). These diffraction peaks are indexed to the akthenskite compact hexagonal - ε-MnO_2 - phase (JCPDS 30-0820). As a consequence, the XRD results allow to validate the transformation of Mn_3O_4 into ε-MnO_2 for high Mn loading. It is also interesting to note that the mean size of the nanocrystal (9 nm, as evaluated by XRD) remains unchanged after acid treatment.

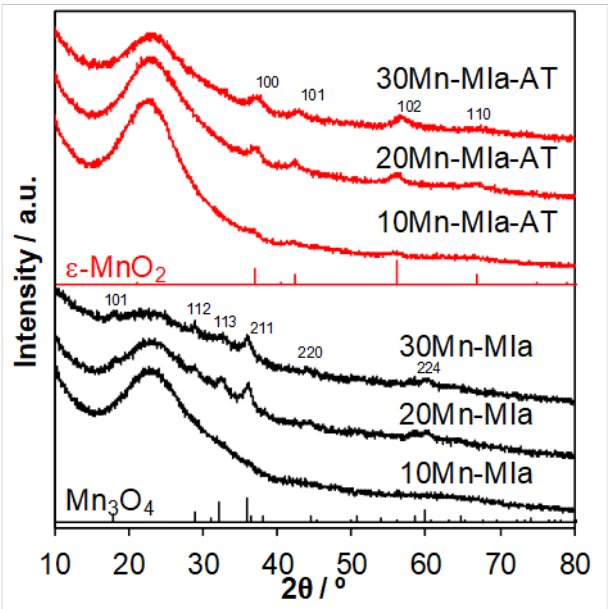

Figure 1. Wide-angle XRD patterns recorded for the xMn-MIa and xMn-MIa-AT samples.

3. Textural properties - N_2-physisorption

The nitrogen adsorption and desorption isotherms recorded at -196°C for the non-calcined SBAa and calcined SBAc supports are shown in **Figure S1**. Both supports exhibit type IV isotherms with H1 hysteresis, corresponding to ordered mesoporous materials with narrow pore size distribution of cylindrical pores centered at 6.6 and 7.3 nm for SBAa and SBAc, respectively (**Figure S2**).
As expected the SBAa sample has a lower S_{BET}, pore volume and maximum pore size than SBAc due to the presence of the template P123 inside the silica porosity. Nitrogen isotherms of the fresh and acid-treated catalysts are given in **Figures S3 - S5**. All the studied catalysts exhibit isotherms of type IV. The Mn 10 wt% based catalysts are characterized by a H1 hysteresis loop. For higher Mn loading, N_2 adsorption/desorption experiments performed on these materials result in a step-wise desorption isotherm, while the adsorption branch shows only one step. The trace of the desorption isotherm can be herein explained by a "pore network effect" [32]. This effect occurs when interconnected larger pores have to empty through pores with a smaller diameter. The step-wise desorption isotherm can be explained considering that encapsulated mesopores empty at lower pressure than the open pores of similar size. These encapsulated mesopores (**Figure S6**) result from the confinement of MnO_x particles at two different locations in the same mesoporous channel interconnected to another open mesoporous channel via a microchannel as previously reported in the literature [32] [33]. The pore volume - pore diameter (**Figures S7 – S9**) representation exhibits an additional pore contribution with a mean diameter of 4.8 nm for Mn 20-30 wt % loadings compared to that of 10 wt% highlighting the "pore network effect".
Plot of the A/(A+B) ratio (see **Figure S4** for the signification of A and B) as a function of Mn loading is shown in **Figure S10**. It is found a linear increase of this ratio with Mn content stressing the increase of the "pore network effect" with manganese content. The accessible specific surface area per gram of SiO_2 decreases by 19 % (10Mn-MIa) while only a 11 % - 13% decrease is observed for the 20Mn-MIa and 20Mn-MIa samples, respectively. These results show that higher Mn (20-30 wt%) loadings do not have a negative effect on the specific surface area of the support. Such observations qualitatively hold for the porous volume.
After acidic treatment, the amount of adsorbed N_2 increases as well as the total pore volume while the nature of the isotherms and the characteristics of the hysteresis loop keep practically unchanged. Additionally, the A/(A+B) ratio increases twice as fast than the one for the fresh catalysts consistent with a beneficial "pore network effect". Microporosity improvement is also highlighted by an increase of Vμ by a factor of about 3-4 due to the removal of surfactant degradation products. To sum up, an improvement of the textural properties of the Mn based samples is clearly observed after acid treatment, which could be obviously related to the decrease in global manganese loading in final materials.

4. Surface properties – X-ray photoelectron spectroscopy

The XPS technique was used to provide information of the effect of acid treatment on the changes in surface chemistry for the Mn based catalysts with Mn content higher than 10 wt%.
Regarding the fresh samples, the XPS Si 2p spectra (**Figure S11**) are dominated by a large symmetrical peak located at a BE of 103.8 eV ± 0.2 eV, characteristic of Si^{4+} in SiO_2. It is found no peak at a BE of 105.2 eV generally attributed to Si-OH bonding [34] [35]. It should be noted that the Mn/Si atomic ratios extracted from the Mn 2p and Mn 3s core-levels (**Table 2**) are significantly lower than those given by ICP in line with infiltrated MnO_x particles inside the SBA-15 porosity [36]. The superposition of the spectra of Mn 3s core level are shown in **Figure S12**. Two peaks are observed due to the coupling of non-ionized 3s electron with 3d valence-band electrons and from the energy difference of these two peaks it is possible to estimate a Mn AOS [37]. It is found that the energy difference decreases after acid treatment in accordance with an increase of the Mn AOS. The Mn AOS values of 2.3 - 2.4 estimated for the fresh catalysts are somewhat lower than that of 2.7 expected for Mn_3O_4 particles reveals the presence of reduced Mn species in the depth of XPS detection. The surface reduction can be explained by the formation of gaseous organic products, in the course of the calcination that can act as reductants towards surface Mn species, as already discussed. The Mn $2p_{3/2}$ envelope has been also decomposed considering a mixture of Mn(II) and Mn(III) which can be formally simulated by a mixture of MnO and Mn_2O_3 in accordance with the fits of M. Biesinger et al. [38] using namely two sets of multiplet peaks having fixed relative intensity, FWHM (adapted for the passing energy used herein) and differing in BE each other by a fixed difference (**Table S1**). For the MnO component, besides the set of 5 peaks, an additional sixth component is added ascribed to the MnO satellite whose FWHM is also left to vary. Except this parameter, it turns out that the only parameter left to modify is the position in BE of the peak located at the lowest BE for each multiplet. Such an approach allows to get correct simulations as shown by the good fitting of the global Mn $2p_{3/2}$ experimental envelope by that of the simulated one as observed in **Figure S13** for the fresh 20Mn-MIa sample. The fitting BEs of the first peak of each set are reported in **Table 2**. Based on the obtained Mn^{2+} and Mn^{3+} relative amounts (**Table 2**) a derived Mn AOS of 2.3 and 2.2 can be obtained for 20Mn-MIa and 30Mn-MIa, respectively. These values

are in accordance with those extracted from the Mn 3s core-level within the margin of uncertainty.

When considering the acid-treated catalysts it is found that the Mn/Si atomic ratios are again significantly lower than those obtained by ICP attesting of the presence of MnO_x particles mostly incorporated in the channels of the silica. However, the Mn AOS, estimated from the Mn 3s core level, rises now up to 3.2 and 3.3 for the acid-treated 20Mn-MIa and 30Mn-MIa samples, respectively. Taking into account the dismutation of Mn(III), the Mn $2p_{3/2}$ envelope has been simulated this time considering a mixture of Mn(II) and Mn(IV) using again the given parameters of Biesinger for MnO and MnO_2 as benchmarks for Mn(II) and Mn(IV) (**Table S2**). The procedure of simulation based on these two sets of multiplet (6 peaks for Mn(II) incorporating the MnO satellite; 6 peaks for Mn(IV)) has been therefore performed adopting the same type of constraints as exposed above for the simulated Mn $2p_{3/2}$ of 20Mn-MIa. Here the Mn 2p envelopes can be successfully simulated considering the overlapping of Mn(II) and Mn(IV) components as shown for 20Mn-MIa-AT (**Figure S14**). The resulting Mn AOS are 3.5 and 3.3 for 20Mn-MIa-AT and 30Mn-MIa-AT samples, respectively. The values are in the same order of magnitude than those issued from the Mn 3s core-level, the obtained value associated for 20Mn-MIa-AT being slightly higher than the one obtained for the fresh sample.

These Mn AOS values are however less than the expected value of 4.0 owing to the formal **Equation 1**. Although the dismutation of Mn(III) into Mn(II) and Mn(IV) occurs quantitatively, the presence of Mn(II) as an extra component can be due to the presence of Mn(II) related species in strong interaction with the support or/and of Mn(II) stabilized in an amorphous or well dispersed MnO_x matrix such as Mn_5O_8 ($Mn_3^{4+}Mn_2^{2+}O_8$).

Table 2: XPS data of the xMn-MIa and xMn-MIa-AT samples

Samples	Si 2p / eV	Mn 2p / eV	Mn AOS [a]	Mn AOS [b]	Mn / Si [a]	Mn / Si [b]	Mn / Si [c]
20Mn-MIa	103.6	640.9 [d] - 641.2 [e]	2.3	2.3	0.118	0.090	0.27
30Mn-MIa	103.5	641.0 [d]– 641.5 [e]	2.2	2.4	0.187	0.144	0.47
20Mn-MIa-AT	103.9	640.6 [f] – 641.8 [g]	3.5	3.2	0.013	0.018	0.10
30Mn-MIa-AT	103.9	640.6 [f] – 641.8 [g]	3.3	3.3	0.069	0.053	0.13

[a] : from XPS (Mn 2p) ; [b] : from XPS (Mn 3s) ; [c] : from ICP ; [d], [e]: MnO-Mn_2O_3 1st peak BE ; [f], [g]: MnO-MnO_2 1st peak BE

5. Redox properties – H_2-Temperature programmed reduction

The H_2-TPR reduction profiles for the fresh and acid-treated samples obtained after a pre-treatment in flowing dry air at 150 °C for 2 h are showed in **Figures S15-S17** and the resulting H_2 consumptions and derived Mn AOS are compiled in **Table S3**. The H_2 consumption trace for all the fresh catalysts shows 2 overlapping peaks centred at 330 °C (± 17 °C) and 472 °C (± 5 °C). For the 10Mn-MIa sample, on contrary to the other ones, the peaks are broad with low intensity in line with a residual H_2 consumption. Attempt to quantify the amount of consumed H_2 allows to get a Mn AOS of 2.1. This low Mn mean valence is likely the consequence of the high initial P123/Mn weight ratio induced by the experimental procedure. Hence, during the calcination the P123 degradation products act as reductants, precluding the oxidation of manganese to MnO_2 as generally expected for a calcination at 300°C. Such a Mn AOS value stresses the possibility of the existence of manganese as MnO particles more or less in interaction with the support and/or as partly incorporated into silica framework. Few studies reported on Mn^{2+} to be substituted for Si^{4+} in the framework position of SBA-15 [39] [40]. However, the use of high pH seems to be a prerequisite for such incorporation [39] which is herein not our case. By opposition, it is found an increase of the global H_2 uptake with Mn content for the two remaining samples consistent with the decrease of the initial P123/Mn weight ratio. The estimated Mn AOS for 30Mn-MIa and 20Mn-MIa are 2.7 and 2.6, respectively. These values agree well with the one of 2.7 expected for the presence of the sole Mn_3O_4 phase consistent with XRD data but in contradiction with the presence of two H_2 consumption peaks as the transformation of Mn_3O_4 into MnO occurs in one step [41] [42]. These conflicting results can be rationalized considering that the two overlapping peaks attest of two locations for the Mn_3O_4 particles [43]. Anyhow, the peak of H_2 consumption at high temperature (HT) increases for 30Mn-MIa.

By opposition, the H_2-TPR profiles are very similar for all samples after acidic treatment followed by calcination at 300°C. Two reduction peaks are observed in the 290-305 °C (LT) and 405-425 °C (HT) temperature range which can be attributed to the successive reductions of MnO_2 into Mn_2O_3/Mn_3O_4 and of Mn_3O_4 to MnO [44] [45] [46]. This assumption is supported by the estimated Mn AOS value of 3.8 (± 0.1) for 30Mn-MIa-AT. By opposition the Mn AOS are significantly lower, namely 3.5 and 3.2 for 10Mn-MIa-AT and 20Mn-MIa-AT samples, respectively although the presence of ε-MnO_2 is clearly observed by XRD. As mentioned before, the presence of MnO particles in strong interaction with the support or/and some metastable amorphous Mn_5O_8 could account for such discrepancies. In addition, some remaining carbon in the xMn-MIa samples may contribute to some extent to these lower Mn AOS values. To check this hypothesis a TGA/DSC experiment has been performed on the 20Mn-MIa sample and the resulting curves are displayed in **Figure S18**. The estimated carbon content is about 3 wt% based on the weight loss in the temperature range of 100 °C and 600 °C (B region in **Figure S18**). This carbon amount is higher than that of Mn (2.4 wt%) for 10Mn-MIa. However, it is strongly suggested that such amorphous carbonaceous residues may have been removed in the course of the acid treatment [47].

For 10Mn-MIa, as 90% of Mn is considered as Mn(II), the role of the acid treatment is mainly to solubilize the manganese species as Mn^{2+}(aq). As the remaining carbon content in the 20Mn-MIa sample is rather low, of 3 wt%, compared to 30 wt% in SBAa from which the Mn precursor has been added, it is speculated that the Mn oxidation is not impeded by the presence of substantial amount of carbon. In this case, the calcination of MnO_x can result to the formation of ε-MnO_2 particles in the channels of SBA-15.

For the 20Mn-MIa and 30Mn-MIa samples the role of acid treatment is to induce the dismutation of Mn(III) in Mn_3O_4 to MnO_2 and Mn^{2+}(aq). The relative weight losses are in accordance with the stoichiometry of such reaction. However, some Mn(II) entities could be stabilized through solubilisation/precipitation processes leading to the formation after calcination of some metastable Mn_5O_8 (20Mn-MIa).

6. Morphology properties – High resolution transmission electron microscopy

TEM and HR-TEM have been used in order to have a comprehensive view of the micro and nanostructure of the samples. Typical images for the fresh and acid treated 10Mn-MIa and 20Mn-MIa samples are displayed in **Figures S19 - S20.** Regarding the 10Mn-MIa sample the TEM image along to pore axis clearly shows that the MnO_x particles are in the channels of the silica and not at the external surface of silica. Consequently, it was concluded that the particles have been successfully entrapped inside the silica channels. Additionally the TEM images normal to pore axis for 10Mn-MIa sample shows few channels covered by MnO_x hollow cylinders shaped particles with a mean thickness of 2.5 ± 0.5 nm. The MnO_x particle length distribution shows a maximum for length in the range 5-7 nm (see **Figure S19**). For 20Mn-MIa, the typical TEM image along to pore axis also shows a uniform distribution of the particles throughout the silica grains. The TEM image normal to pore axis reveals, contrarily to the previous sample, some occluded channels and a higher density of hollow cylinders shaped particles. The more common associated lengths shift to higher values: 7-9 nm compared to 5-7 nm observed for 10Mn-MIa.

On contrary to the previous images, the TEM image of the acid-treated 10Mn-MIa sample reveals some agglomerated nanotube shaped MnO_x particles (5-30 nm length and less than 10 nm diameter) at the external surface of silica along with those always entrapped in the silica channels having a narrower cylinder length distribution in the 3-7 nm range (**Figure S20**). By opposition, no such observation can be made for the 20Mn-MIa-AT sample. The homogeneous distribution of the hollow cylinder shaped particles is preserved. Furthermore, the most common particle lengths shift to lower value indicating that the acid treatment induces globally a decrease in the size of the MnO_x particles.

7. Catalytic properties – HCHO total oxidation

The HCHO oxidation light-off curves for the different catalysts are reported in **Figure 2** and the resulting catalytic performances are gathered in **Table S4**. Based on the T50 (°C) value, the fresh catalysts can be ranked by decreasing activity as follows: 30Mn-MIa (141) ≈ 20Mn-MI-a (144) > 10Mn-MIa (183). These results show that the HCHO activity significantly increases up to 20 wt% Mn and that a further increase of Mn loading does not improve it. After acid treatment, it is found that the light-off curve for 10Mn-MIa-AT is slightly shifted to higher temperature compared to that for the fresh one (T_{50} increase by about 30 °C) while those for higher Mn contents are shifted to lower temperatures (T_{50} and T_{90} decrease by about 20 °C). To get a more accurate comparison of catalytic activity taking into account that the acid treatment results in a release of manganese into solution, a standardized rate rs of HCHO conversion into CO_2 per mole of Mn has been calculated at 130 °C (20Mn and 30Mn samples) and at 170°C (10Mn samples considering their lower activity). Taking into account these results, it is found a five-fold and a four-fold increase of rs for 20Mn-MIa-AT and 30Mn-MIa-AT, respectively, compared to the untreated samples. Furthermore, a two-fold increase of rs is also observed for the 10Mn-MIa-AT sample. Hence it is evidenced a beneficial effect of the acid treatment irrespective of the Mn content. The highest value of rs is obtained for the acid-treated 20Mn-MIa catalyst whose value is 51 mmoles of HCHO converted into CO_2 per mole of Mn and per hour.
The positive impact of the acid treatment observed for both catalysts can be partly attributed to improved redox properties. Indeed, the increase of Mn AOS, the easy cycling between Mn^{3+}/Mn^{2+} and Mn^{4+}/Mn^{3+} mixed valences due to the implement of stabilized Mn^{2+} and Mn^{4+} as a direct consequence of the acid treatment contribute to such enhancement. Additionally, a better dispersion of the Mn entities is observed by HR-TEM after acid treatment. Finally, improvement of the textural properties through acid treatment may facilitate oxygen mobility and better diffusion of the reactants.

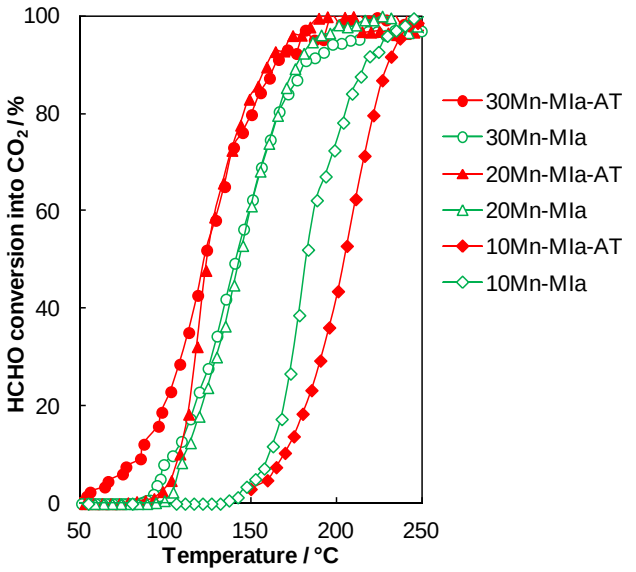

Figure 2: Light-off curves of the xMn-MIa catalysts before and after acid treatment

8. Stability properties – HCHO oxidation under dry and humid air

The effect of humidity (RH = 0%, 50 %) has been investigated on the stability of the 20Mn-MIa-AT catalyst at 130 °C for 70 h. The plots of HCHO conversion as a function of time are exhibited in **Figure S21** and the associated results are given in **Table 3**. Whatever the nature of the gaseous effluent the HCHO conversion as a function of time exhibits two regimes: an important decrease of the HCHO conversion in the first twenty hours followed by a slight linear deactivation. After 70 h, as the remaining activity is quite similar (a_{130} (ratio between the HCHO conversion after 70 h reaction to that at initial time) of 0.19 ± 0.01) in dry and humid air it follows that the catalytic activity of 20Mn-MIa-AT is somewhat higher for RH = 50%.
The XRD patterns of the used catalysts are shown in **Figure S22** to be compared with that of the fresh 20Mn-MIa-AT solid. Irrespective of the water content, the XRD patterns of the used catalysts show 3 broad less intense asymmetric peaks in 2θ

positioned at about 37 °, 42 ° and 56 ° which can be again assigned to ε-MnO_2 but the poor resolution of these reflections cannot ruled out the presence of possible reduced Mn phases such as MnO and/or even Mn_3O_4.
The N_2-isotherms keep their type IV character and the associated hysteresis loops exhibit the same characteristics of "pore network effect" in accordance with the pore size distributions (**Figures S23 – S24**). However, the textural properties of the used catalysts are negatively affected and much more in dry air (**Table 3**).

Table 3: Properties of the fresh and used 20Mn-MIa-AT

Properties	Fresh	Used RH = 0 %	Used RH = 50%
X^{i}_{HCHO} (%)	-	78	100
X^{f}_{HCHO} (%)	-	14	20
a_{130} [a]	-	0.18	0.20
dc (nm)	9	7	10
S_{BET} ($m^2.g_{cat}^{-1}$)	772	486	593
Vp ($cm^3.g_{cat}^{-1}$)	1.09	0.79	0.89
Sμ ($m^2.g_{cat}^{-1}$)	219	136	171
Vμ ($cm^3.g_{cat}^{-1}$)	0.025	0.010	0.018
Mn AOS [b]	3.2	2.4	2.2

[a]: ratio between the HCHO conversion after 70 h reaction to that at initial time; [b]: from H_2-TPR.

Additionally, the redox properties of the used catalysts have been investigated by H_2-TPR experiments and the H_2 consumption profiles are reported in **Figure S25**. On contrary to the H_2-TPR profile of 20Mn-MIa-AT showing two peaks, those of the used catalysts exhibit one peak that could be attributed, due to its position, to the reduction of Mn_3O_4 into MnO. All things being equal otherwise, the relative lower peak intensity observed for 20Mn-MIa-AT-0 (RH = 0%) attests of the presence of more reduced MnO_x species. This is consistent with the estimated Mn AOS of 2.2 and 2.4 for 20Mn-MIa-AT-50 and 20Mn-MIa-AT-0, respectively (**Table 3**), and these results suggest the stabilization of reduced phases of manganese oxide after reaction (under humid and under dry air), not visible by XRD (**Figure S22**).
As reported previously, the catalyst deactivation in dry air condition can be attributed to a poisoning effect due formate species strongly bonded to the manganese active sites [48] [49]-[50]. Such formate species can be observed by FTIR-ATR on the used samples as reported on **Figure S26**. The formation of such formate species from formaldehyde implies the consumption of active oxygen according to the following equation:

$$HCHO(g) + 2O^* \rightarrow HCOO(ad) + OH(ad)$$

Equation 2

This reaction is accompanied with the concomitant reduction of manganese. Hence the most active sites can be readily poisoned in the first stages of the reaction since re-oxidation of some manganese active sites might be impeded by the formed adsorbed formate species at 130 °C. In humid air (RH = 50%), the water is reported to compete with formaldehyde for the adsorption on active sites [51] that can lead to a cleaning of the surface, facilitating the re-oxidation of reduced manganese sites. However, the presence of 50% RH in the feed does not allow to improve the catalyst stability, as observed in **Figure S21**, suggesting that such phenomenon does not positively impact the catalyst properties if it occurs.

Conclusion

To conclude, it is reported a net beneficial effect, in terms of catalytic performances, of a HNO_3 10M treatment at 25 °C on reduced MnO_x particles incorporated in the porous channels of a mesoporous silica through melt infiltration whatever the Mn content ranging from 10 to 30 wt%. Promotion of the redox properties, enhancement of the active phase dispersion and improvement of the textural properties can account for these better catalytic activities obtained over acid treated catalysts.

Experimental Section

Support preparation

As made silica (SBAa) support was synthesized according to the procedure proposed by Zhao et al. [52] 4 g of Pluronic P123 (poly(ethylene oxide)-block-poly(propylene oxide)-block-poly(ethylene oxide)- block, PEO20–PPO70–PEO20, with MW = 5800 g. mol^{-1}) was dissolved in a 1.6 M solution of HCl at 40 °C. 8.5 g of a silica precursor, tetraethyl orthosilicate (TEOS), was added dropwise to the solution, followed by magnetic stirring for 24 h. The resulting gel was subjected to hydrothermal treatment for 48 h at 100 °C. After recovering by filtration, washing, and drying, the material was used as support. Calcination of SBAa in static air at 550°C for 6 h (1.5 °C.min^{-1}) led to the SBAc support.

Catalyst preparation

The modified MI was performed using manganese nitrate tetrahydrate as Mn(II) precursor and SBAa as host support [16] [18] [19] [20] . The Mn solid was previously grounded with the SBAa support in a proper ratio to get different Mn contents (10, 20 and 30 wt%) at room temperature for 15 minutes. The solid mixture was then heated in a Teflon autoclave of 100 mL at 38 °C for 12 days. The solid was finally calcined in static air at 300 °C for 6 h (1.5 °C.min^{-1}). The samples were labelled xMn-MIa with x as weight percentage of Mn.

Acid treatment

About 500 mg of xMn-MIa samples were suspended in an aqueous HNO_3 solution (50 mL; 10 mol.L−1) under constant stirring for 5 hours at ambient temperature. After centrifugation, the suspensions were filtered, washed with water and dried at 80 °C. Finally, the powders were calcined at 300 °C for 6 h (1.5 °C.min-1). The samples were labelled xMn-MIa-AT (AT: Acid-treated).

Catalyst Characterization

XRD measurements were carried out with a Bruker D5000 vertical goniometer equipped with Cu anode (Kα radiation λ=1.5418 Å). A proportional counter and a 0.04° step size in 2θ were used. The integration time was 2 seconds per step and the scan range was from 10 to 80° in 2θ. The assignment of the various crystalline phases was based on the comparison with files in PDF card (Powder Diffraction Files structure data base). The mean crystallite size (dc) of MnO_x phase was calculated from the line broadening of the most intense reflection using the Scherrer equation.

N_2 adsorption-desorption isotherms were measured at 77K, using a gas adsorption analyzer (TriStar II 3020). Pore volume was determinate at P/P_0 = 0.99. The BET method was used to calculate the specific surface areas. The microporous surfaces and volumes were determined from the t-plot method. Pore size distribution was determined using the Barrett-Joyner-Halenda (BJH) model, applied to the desorption branch. The sample was heated at 100°C for 3 hours under vacuum before measurement.

IR-ATR (infra-red attenuated total reflectance) spectra were collected using a Thermo scientific iS50 spectrometer equipped with a triglycine sulfate (TGS) detector (spectral resolution: 4 cm^{-1}).

Redox properties of the samples were evaluated using a conventional temperature-programmed reduction apparatus (Micromeritics model AutoChem II). 50 mg of the sample was placed in a quartz reactor and heated in flowing air (50 $mL.min^{-1}$) at 150 °C and then cooled down to room temperature. Then the reactor was heated from 25 °C to 1000 °C with a heating rate of 10 °C min^{-1} in a gas mixture (5 vol.% H_2 + 95 vol.% Ar, 50 $mL.min^{-1}$). Quantification of H_2 consumption was assessed using a TCD.

The Mn AOS was estimated from the following equation:

$$Mn\ AOS = 2 + 2 \times (n_{H2} / g) / (n_{Mn} / g) \qquad \textbf{Equation 3}$$

TGA (Thermo-Gravimetric Analysis) / DSC (Differential Scanning Calorimetry) measurements were performed using a Balance TA Instrument (SDT 2960 DSC-TGA X). The analysis was performed under 20 $\%O_2$/He flow (100 $mL.min^{-1}$) in the temperature range 25 - 800 °C (10 °$C.min^{-1}$).

Elemental analyses were performed by inductively coupled plasma-optic emission spectroscopy 720-ES ICP-OES (Agilent) with axially viewing and simultaneous CCD detection. The sample preparation was made by dissolving 10 mg of dried and ground sample catalyst in 1.5 mL of concentrated nitric acid and 500 µL of hydrofluoric acid solution. Solutions were heated at 50 °C and stirred for 24 hours in a sonication bath.

The X-ray photoelectron spectroscopy (XPS) analyses were performed with a Kratos Axis Ultra system. As excitation source was used the unmonochromatized Al Kα radiation (1486.6 eV). The sample powders were analysed as pellets, mounted on a double-sided adhesive tape. The pressure in the analysis chamber was in the range of 10-9 mbar during data collection. The binding energies of the different core levels were referred to the C1s component set at 284.8 eV. Atomic concentrations were calculated from peak intensity using the sensitivity factors provided with the software. The binding energy (BE) values are quoted with a precision of ± 0.15 eV and the atomic percentage with a precision of ± 10 %.

The high-resolution transmission Electronic Microscopy (HRTEM) were performed on a JEOL 2100 instrument (200 kV; LaB6 source ; a Gatan Ultra scan camera) equipped with a Hypernine (Premium) detector (active area: 30 mm^2). Before analysis, the samples were embedded in a resin and sliced using an ultramicrotome (cuts of ~100 nm thick).

The catalytic oxidation of formaldehyde was performed in a fixed-bed reactor (internal diameter = 10 mm) loaded with 200 mg of catalyst as our previous report18. Before each test, the catalyst was treated 1 hour at 300°C in O_2 (20 vol.%)/N_2 flow (100 $mL.min^{-1}$). 100 ppmv of gaseous formaldehyde in air (100 $mL.min^{-1}$) generated from para-formaldehyde in a permeation tube placed in a permeation chamber (Dynacalibrator, VICI Metronics Inc.) was allowed to flow through the catalyst. The reactor temperature was decreased at 0.5 °$C.min^{-1}$ from 300 °C to 100 °C and at 0.2 °$C.min^{-1}$ from 100 °C to 20 °C in the course of the reaction.

The effluent gases were analysed online with a Varian CP-4900 Micro-GC equipped with a thermal conductivity detector and COX type column (1m).

The formaldehyde conversion (X_{HCHO}, %) was evaluated using the following equation:

$$X_{HCHO}\ (\%) = [CO_2] / [HCHO]_{ini} \qquad \textbf{Equation 4}$$

Where $[CO_2]$ was the concentration of CO_2 at time t and $[HCHO]_{ini}$ the initial concentration of formaldehyde.

A test of durability was performed at 130 °C for 70 hours in dry air and moist air (RH = 50%) using the same experimental conditions as those given above. To quantify the resistance against deactivation an activity coefficient a130 was defined as the ratio between the HCHO conversion after 70 h reaction to that at initial time.

Acknowledgements

This research is supported by a European Program INTERREG V France—Wallonie—Flanders (FEDER) (DepollutAir). Chevreul institute (FR 2638), Ministère de l'Enseignement Supérieur et de la Recherche and Région Hauts-de-France are also acknowledged for supporting this work. ICP analyses were performed in the « Spectrométrie par torche à plasma » platform of the Research Federation Michel-Eugène Chevreul hosted by the LASIR laboratory. The authors thank Adrian Ungureanu (TU Iasi – RO) and Carmen Ciotonea (Université de Lille - UCCS UMR 8181 CNRS - FR) for the synthesis of the materials, Martine Trentesaux and Pardis Simon, Olivier Gardoll and Laurence Burylo for their contribution in XPS, H_2-TPR and XRD measurements, respectively.

Keywords: Volatile organic compound • formaldehyde • catalytic oxidation • porous materials • manganese oxide • acidic treatment

[1] IARC, In: *IARC Monographs on the Evaluation of the Carcinogenic Risk of Chemicals to Humans.* IARC (International Agency Res. Cancer) **1982**, 29, 345–389.
[2] Torres, J. Q.; Royer, S.; Bellat, J. P.; Giraudon, J. M.; Lamonier, J. F. *ChemSusChem* **2013**, 6 (4), 578–592.
[3] Yan, Z.; Xu, Z.; Yu, J.; Jaroniec, M. *Environ. Sci. Technol*. **2015**, 49 (11), 6637–6644.
[4] Zhang, C.; Li, Y.; Wang, Y.; He, H. *Environ. Sci. Technol*. **2014**, 48 (10), 5816–5822.
[5] Xu, Q.; Lei, W.; Li, X.; Qi, X.; Yu, J.; Liu, G.; Wang, J.; Zhang, P. *Environ. Sci. Technol*. **2014**, 48 (16), 9702–9708.
[6] Sekine, Y. *Atmos. Environ*. **2002**, 36 (35), 5543–5547.
[7] Bai, B.; Qiao, Q.; Arandiyan, H.; Li, J.; Hao, J.. *Environ. Sci. Technol*. **2016**, 50 (5), 2635–2640.
[8] Liu, L.; Tian, H.; He, J.; Wang, D.; Ma, C.; Yang, Q. *J. Nanosci. Nanotechnol*. **2015**, 15 (4), 2887–2895.
[9] Pang, G.; Wang, D.; Zhang, Y.; Ma, C.; Hao, Z. *Front. Environ. Sci. Eng*. **2016**, 10 (3), 447–457.
[10] Bai, B.; Qiao, Q.; Li, J.; Hao, J. *Chinese J. Catal*. **2016**, 37 (1), 27–31.
[11] Wang, J.; Li, J.; Zhang, P.; Zhang, G. *Appl. Catal. B Environ*. **2018**, 224 (August 2017), 863–870.
[12] Miyawaki, J.; Lee, G.; Yeh, J.; Shiratori, N.; Shimohara, T.; Mochida, I.; Yoon, S. *Catal. Today* **2012**, 185 (1), 278–283.
[13] Fang, R.; Huang, H.; Ji, J.; He, M.; Feng, Q.; Zhan, Y.; Leung, D. Y. C. *Chem. Eng. J.* 2018, 334, **2017**, 2050–2057.
[14] De Jongh, P. E.; Eggenhuisen, T. M. *Adv. Mater*. **2013**, 25 (46), 6672–6690.
[15] Yin, Y.; Yang, Z.-F.; Wen, Z.-H.; Yuan, A.-H.; Liu, X.-Q.; Zhang, Z.-Z.; Zhou, H. *Sci. Rep*. **2017**, 7 (1), 4509.

[16] Ciotonea, C.; Mazilu, I.; Dragoi, B.; Catrinescu, C.; Dumitriu, E.; Ungureanu, A.; Alamdari, H.; Petit, S.; Royer, S. *ChemNanoMat* **2017**, 3 (4), 233–237.
[17] Dragoi, B.; Mazilu, I.; Chirieac, A.; Ciotonea, C.; Ungureanu, A.; Marceau, E.; Dumitriu, E.; Royer, S. *Catal. Sci. Technol*. **2017**, 7 (22), 5376–5385.
[18] C. Ciotonea, B. Dragoi, A. Ungureanu,* E. Marceau, H. Alamdari, S. Petit, E. Dumitriu, S. Royer, *Catalysis Science & Technology* **2017**, 7, 5448-5456.
[19] S. Chen, C. Ciotonea, A. Ungureanu, E. Dumitriu, C. Catrinescu, R. Wojcieszak, F. Dumeignil, S. Royer, *Catal. Today* **2019**, in press.
[20] Rochard, G.; Ciotonea, C.; Royer, S.; Giraudon, J.-M.; Lamonier, J.-F. *ChemCatChem* **2019** in press.
[21] Dent Glasser, L. S.; Smith, I. B. *Mag. J. Mineral. Soc*. **1968**, 36 (283), 976–987.
[22] López-Fonseca, R.; Elizundia, U.; Landa, I.; Gutiérrez-Ortiz, M. A.; González-Velasco, J. R. *Appl. Catal. B Environ*. **2005**, 61 (1–2), 150–158.
[23] Atribak, I.; Bueno-López, A.; García-García, A.; Navarro, P.; Frías, D.; Montes, M. *Appl. Catal. B* Environ. **2010**, 93 (3–4), 267–273.
[24] Averlant, R.; Royer, S.; Giraudon, J. M.; Bellat, J. P.; Bezverkhyy, I.; Weber, G.; Lamonier, J. F. *ChemCatChem* **2014**, 6 (1), 152–161.
[25] Ohzuku, T.; Higashimura, H.; Hirai, T. *Electrochim. Acta* **1984**, 29 (6), 779–785.
[26] Sinha, A. K.; Suzuki, K.; Takahara, M.; Azuma, H.; Nonaka, T.; Suzuki, N.; Takahashi, N. *J. Phys. Chem. C* **2008**, 112 (41), 16028–16035.
[27] Beley, M.; Brenet, J. *Electrochim. Acta* **1973**, 18 (12), 1003–1011.
[28] Das, M.; Bhattacharyya, K. G. *Chem. Eng. Commun*. **2014**, 202 (12), 1657–1667.
[29] Quiroz, J.; Giraudon, J.-M.; Gervasini, A.; Dujardin, C.; Lancelot, C.; Trentesaux, M.; Lamonier, J.-F. *ACS Catal*. **2015**, 5 (4), 2260–2269.
[30] Torres, J. Q.; Giraudon, J.-M.; Lamonier, J.-F. *Catal. Today* **2011**, 176 (1), 277–280.
[31] Ciotonea C., Averlant R., Rochard G., Mamede A.-S., Giraudon J.-M., Alamdari H., Lamonier J.-F. and Royer S., *ChemCatChem* , **2017**, 9, 2275-2283
[32] Ravikovitch, P. I.; Neimark, A. V. *Langmuir* **2002**, 18 (25), 9830–9837.
[33] Sietsma, J. R. A.; Meeldijk, J. D.; Versluijs-Helder, M.; Broersma, A.; Jos Van Dillen, A.; De Jongh, P. E.; De Jong, K. P. *Chem. Mater.* **2008**, 20 (9), 2921–2931.
[34] Paparazzo, E. *Appl. Surf. Sci*. **1993**, 72 (4), 313–319.
[35] Paparazzo, E. *Interface Anal*. **1996**, 24 (10), 729–730.
[36] Ungureanu, A.; Dragoi, B.; Chirieac, A.; Ciotonea, C.; Royer, S.; Duprez, D.; Mamede, A. S.; Dumitriu, E. *ACS Appl. Mater. Interfaces* **2013**, 5 (8), 3010–3025.
[37] Galakhov, V. R.; Demeter, M.; Bartkowski, S.; Neumann, M.; Ovechkina, N. A.; Kurmaev, E. Z.; Lobachevskaya, N. I.; Mukovskii, Y. M.; Mitchell, J.; Ederer, D. L. *Phys. Rev. B* **2002**, 65 (11), 113102.
[38] Biesinger, M. C.; Payne, B. P.; Grosvenor, A. P.; Lau, L. W. M.; Gerson, A. R.; Smart, R. S. *Appl. Surf. Sci*. **2011**, 257 (7), 2717–2730.
[39] Kumar, G. S.; Palanichamy, M.; Hartmann, M.; Murugesan, V. *Microporous Mesoporous Mater*. **2008**, 112 (1–3), 53–60.
[40] Selvaraj, M.; Sinha, P. K.; Lee, K.; Ahn, I.; Pandurangan, A.; Lee, T. G. *Microporous Mesoporous Mater*. **2005**, 78 (2–3), 139–149.
[41] Bulavchenko, O. A.; Venediktova, O. S.; Afonasenko, T. N.; Tsyrul'nikov, P. G.; Saraev, A. A.; Kaichev, V. V.; Tsybulya, S. V. *RSC Adv*. **2018**, 8 (21), 11598–11607.
[42] Zengjian, Z.; Hui, W.; Guofeng, G. *IEEE*, **2011**; pp 1994–1997.
[43] Han, Y.; Chen, F.; Zhong, Z.; Ramesh, K.; Chen, L.; Widjaja, E. *J. Phys. Chem*. B **2006**, 110 (48), 24450–24456.
[44] Tian, H.; He, J.; Liu, L.; Wang, D.; Hao, Z.; Ma, C. *Microporous Mesoporous Mater*. **2012**, 151, 397–402.
[45] Wang, J.; Li, D.; Li, P.; Zhang, P.; Xu, Q.; Yu, J. *RSC Adv*. **2015**, 5 (122), 100434–100442.
[46] Zhang, J.; Li, Y.; Wang, L.; Zhang, C.; He, H. *Catal. Sci. Technol*. **2015**, 5 (4), 2305–2313.
[47] Hitz, S.; Prins, R. *Catalysts. J. Catal*. **1997**, 168, 194–206.
[48] Zhao, D. Z.; Shi, C.; Li, X. S.; Zhu, A. M.; Jang, B. W. L. *J. Hazard. Mater*. **2012**, 239, 362-369.
[49] Fan, Z.; Zhang, Z.; Fang, W.; Yao, X.; Zou, G.; Shangguan, W. *Chinese J. Catal*. **2016**, 37 (6), 947‑954.
[50] Qi, L.; Cheng, B.; Yu, J.; Ho, W. *J. Hazard. Mater*. **2016**, 301, 522–530.
[51] Wang, J.; Zhang, P.; Li, J.; Jiang, C.; Yunus, R.; Kim, J. *Environ. Sci. Technol*. **2015**, 49 (20), 12372–12379.
[52] Zhao, D. *Pores. Science*. **1998**, 279 (5350), 548–552.

Entry for the Table of Contents

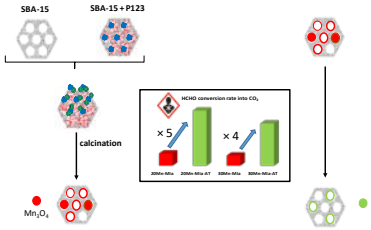

Reduced MnO_x particles (Mn : 10, 20, 30 wt %) incorporated in the porous channels of a mesoporous silica (SBA-15) through melt infiltration were treated with HNO_3 at 25 °C. The results have shown that promotion of the redox properties, enhancement of the active phase dispersion and improvement of the textural properties over acid treated catalysts contribute for the enhancement of the catalytic performances.